JOURNAL OF PROPULSION AND POWER
Vol. 21, No. 4, July–August 2005

Effect of Rocket Exhaust Configurations on Ejector Performance in RBCC Engines

J. Etele* and J. P. Sislian†
University of Toronto Institute for Aerospace Studies, Toronto, Ontario M3H 5T6, Canada
and
B. Parent‡
Seoul National University, 151-744, Republic of Korea

The results of a study of several rocket-based combined cycle engine ejector flowfield configurations, those using a single rocket located along the axisymmetric axis and those incorporating an additional annular rocket located along the outer wall of the ejector are detailed. Steady-state solutions of the axisymmetric Favre averaged Navier–Stokes equations closed by the Wilcox k–ω turbulence model (including the Wilcox dilatational dissipation correction) are obtained using WARP, a finite difference flow solver using the Yee–Roe flux limiting scheme. It is shown that by having 75% of the rocket exhaust enter the ejector through the annular rocket a compression ratio of nearly 2.5 can be achieved for the case where both the air and rocket exhaust mass flows are equal. It is also shown that the effectively mixed area using this configuration extends over the outer 95% of the ejector exit area. A grid convergence analysis shows the resulting total pressure increase to be conservative by approximately 10%. In addition, WARP's ability to simulate mixed subsonic/supersonic shear layers accurately with high convective Mach numbers is demonstrated through comparison with experimental data.

Nomenclature

A = area
a = speed of sound
C_p = specific heat at constant pressure
c = mass fraction
E = specific total energy
e = specific internal energy
h = specific enthalpy
k = specific turbulence kinetic energy
M = Mach number
$\mathcal{M}$ = molecular weight
$\dot{m}$ = mass flow rate
Pr = Prandtl number
p = pressure
R = gas constant
$\bar{R}$ = universal gas constant, 8.314 kJ/kmol · K
Sc = Schmidt number
T = temperature
u = streamwise velocity component
v = radial velocity component
α = air/rocket mass flow ratio
β = mixing parameter
γ = ratio of specific heats
δ = boundary-layer height
ε_d = dilatational dissipation correction
ε_s = solenoidal dissipation
ζ = rocket/air total pressure ratio
θ = air/rocket specific total enthalpy ratio
κ = heat transfer coefficient
μ = viscosity coefficient
ν = diffusion coefficient
π_e = compression ratio, p_e^0/p_a^0
ρ = density
σ = rocket exhaust/ejector inlet area ratio
τ = stress
ϕ = equivalence ratio
ω = dissipation rate per unit of k
∞ = freestream

Subscripts

A = annular rocket
a = air
axi = axisymmetric
C = central rocket
c = convective
cr = critical
e = exit
i = inlet
k = species
r = rocket
rel = relative
sl = shear layer
T = turbulent
t = throat
v = viscous
2D = two dimensional

Superscripts

n = iteration level
0 = stagnation conditions
$\sim$ = Favre average
$-$ = Reynolds average
$*$ = sonic conditions or including turbulent effects
† = turbulent co-efficient of viscosity only (μ_T)

Introduction

THE typical rocket-based combined cycle (RBCC) operating cycle consists of from three to four distinct operating modes, 1) ejector, 2) ramjet, 3) scramjet, and 4) rocket, where, depending

---

Received 20 May 2004; revision received 29 November 2004; accepted for publication 23 November 2004.

*Graduate Student, High Speed Vehicle Propulsion Group, 4925 Dufferin Street; jetele@mae.carleton.ca. Member AIAA.

†Professor, High Speed Vehicle Propulsion Group, 4925 Dufferin Street; sislian@caius.utias.utoronto.ca. Associate Fellow AIAA.

‡Research Associate, Department of Aerospace Engineering; bernard@snu.ac.kr.

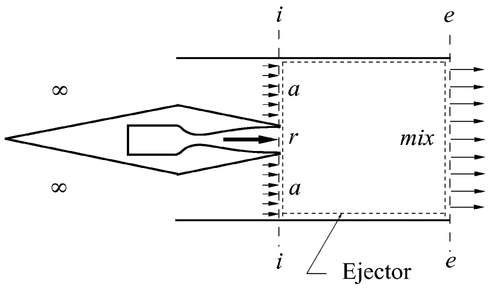

Fig. 1 Ejector section of RBCC engine.

on the overall engine design, the scramjet cycle may or may not be present. Of critical importance during the low speed, low-altitude phases of launch is the ejector operating mode, where the entrainment and subsequent compression of the atmospheric air is largely responsible for any increased performance over traditional rockets. This is accomplished within the ejector section of the engine (Fig. 1), where the high-energy rocket exhaust transfers both its momentum and energy to the entrained airstream.

This mixing and compression process within various types of ejectors has been the subject of research dating back as early as 1949 with the work of von Kármán.[1] Thrust augmenting ejectors, even in applications where they are not part of a combined cycle engine, have been shown to have the potential to improve performance. From a theoretical viewpoint, Alperin and Wu[2,3] studied simplified constant area ejectors that act to entrain and mix atmospheric air with a primary jet (neglecting viscous and blockage losses while assuming complete mixing). After expanding the flow to atmospheric pressure, they show that when compared to the thrust of the primary jet alone (expanded to the same pressure), one can achieve appreciable levels of increased thrust. Dutton and Carroll[4,5] also consider a similar ejector configuration, but with the emphasis being on optimizing not the overall thrust augmentation over the primary jet, but rather on optimizing some of the more common ejector operating parameters such as maximizing the ratio of entrained air to primary jet mass flows α, minimizing the ratio of primary jet to entrained air total pressures ζ, or maximizing the ratio of exit to entrained air total pressures π_e.

The incorporation of the ejector within the larger class of RBCC engine technologies has also been analyzed by numerous researchers. For example, Billig[6] gives a comprehensive analysis of the rocket–ram–scramjet engine, with particular attention paid to a two-dimensional model. These analyses include many of the effects expected to be encountered during the practical implementation of an RBCC engine, including, but not limited to, external drag, inlet design, internal skin friction, and thermal choking. Daines and Segal[7] provide an excellent overview of the critical areas of study concerning RBCC engine design, including a summary of research done up to 1998 in these areas. Recently, theoretical treatment of RBCC engines has progressed to the point where studies examining details as specific as the effect of the molecular weight of the primary jet on overall performance have been performed (Han et al.[8]).

Although almost all research in the area of RBCC design acknowledges that the rocket configuration within the ejector duct can have a significant impact on overall performance, there is little in the way of quantitative evidence testifying to this effect. At Pennsylvania State University, Cramer et al.[9] used hot rocket exhaust combined with diffusion and afterburning in the downstream sections of the engine to compare the effect of using twin thrusters to a single thruster within a rectangular geometry. This study found that the twin thruster configuration could entrain more air, mix in a shorter distance, and produce higher compression ratios than the single thruster alone. West et al.[10] and Ruf[11] examined the Cramer et al. single-thruster configuration using a pressure-based, reacting flow solver incorporating an extended k–ε two-equation turbulence model and a seven-species, nine-reaction H_2/O_2 chemistry model. However, there is no mention beyond that already stated in the experimental results of using different thruster configurations to improve the performance of the ejector.

Daines and Merkle[12] use a pressure-based, finite difference algorithm to solve the Favre averaged Navier–Stokes equations closed by the k–ε turbulence model of Chen and Kim to examine an axisymmetric configuration in which both a single rocket along the duct centerline and an annular rocket placed so as to divide the airflow evenly are compared. Here again the results show a significant increase in the mixing rate when the annular rocket configuration is used. This study goes on to examine the effects of varying parameters such as downstream fuel injection and flight Mach number, but with the focus remaining on the single central rocket configuration.

Over recent years, a significant amount of research has been done on the Aerojet Strutjet, a design that takes full advantage of the increased performance incumbent with rocket segregation. Here, vertical struts, at the end of which are embedded small rockets, are placed within a rectangular ejector section. DeBonis and Yungster[13] have performed a numerical analysis of the inlet section of this design using the NPARC code (albeit with both the embedded rocket and fuel injection ports inoperative) whereas Daines[14] and Daines and Bulman[15] examined a simplified Strutjet design with only a single strut to evaluate the effects of dynamically varying both the rocket exhaust angle and cycle frequency on ejector performance. Numerous other numerical rocket ejector/ducted rocket simulations have been performed[16–20]; however, in each case it is the single-rocket exhaust configuration that is examined.

The objective of the present paper is to consider an axisymmetric ejector and vary the rocket exhaust configuration to quantify the effect this has on two key ejector performance criteria: 1) the overall mixing of the rocket and airstreams and 2) the ratio of the total pressure at the ejector exit to that of the entrained airstream. Ejector configurations in which an annular rocket (located along the outer wall) is used to inject varying percentages of the total rocket exhaust mass flow into the ejector are compared to a configuration in which only a single rocket placed along the axis is used (to show the degree to which rocket placement is effective in increasing ejector performance).

Ejector Theory

There are two main modes of operation for an ejector engine, differentiated by the behavior of the incoming air. During the initial stages of launch when the flight Mach number is subsonic, the incoming air is entrained into the ejector duct by the action of the rocket exhaust. This pumping action acts to increase the total mass flow through the ejector duct, and the engine is said to be operating in ejector rocket mode. However, as the flight Mach number is increased to values beyond Mach one, the air inflow is generally determined by external conditions such as flight Mach number and inlet shock structure (unless at some downstream point within the ejector the conditions are sufficient to unstart the inlet). In this case, the engine is considered to be operating in air augmented rocket or ram rocket mode.

To better understand any computational results obtained, as well as to guide the selection of the conditions under which an ejector will be examined, some theoretical analysis is warranted. From a theoretical standpoint, the calculation of the flowfield during ejector rocket mode poses more of a challenge than during air augmented rocket mode. This is because the entrained airflow Mach number $M_{(a,i)}$ depends on numerous factors within the ejector itself, that is, rocket exhaust conditions, geometry, mixing process, etc. Therefore, this becomes the key unknown parameter required to determine the amount of air being entrained into the engine because in most cases the flight conditions, rocket properties, and overall geometry are known. One method of solving for this parameter is to assume the scenario shown in Fig. 2. In this case, if one assumes that the rocket exhaust expands into the entrained airflow during the initial section of the ejector (by virtue of a higher static pressure), this creates a converging area streamtube into which the subsonic air travels. This in turn creates an aerodynamic throat that can choke the entrained air (barring any downstream conditions that would prevent this), sometimes referred to as a Fabri choke condition. With this assumption, one can avoid having to specify any conditions at the ejector exit since past the choke (or critical) location it is reasonable

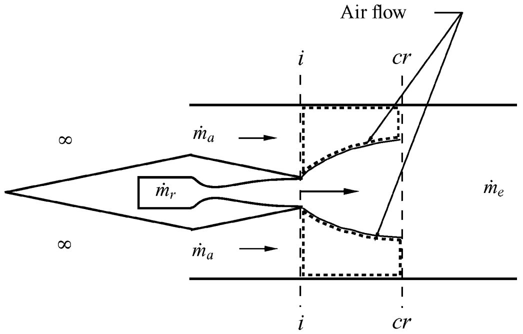

a) Airstream control volume

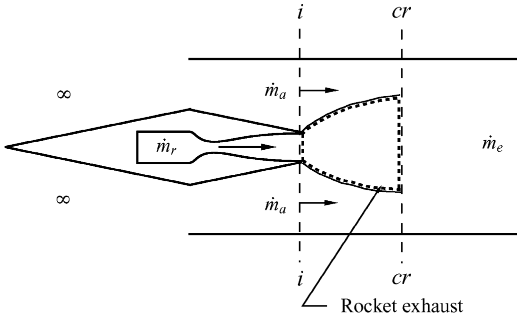

b) Rocket exhaust control volume

Fig. 2 Ejector rocket mode with choked air stream.

to assume that, as the two streams mix, the combination of a sonic airstream and a highly supersonic rocket exhaust stream will result in a supersonic mixed exit flow.

Neglecting the effects of viscosity while assuming that the two streams are uniform and do not mix until the critical station where the airflow chokes, one can write, for a control volume surrounding the rocket exhaust as shown in Fig. 2b,

$$\dot{m}_r u_{(r,i)} + p_{(r,i)} A_{(r,i)} + \int_{sl} p \, \mathrm{d}A - \dot{m}_r u_{(r,cr)} - p_{(r,cr)} A_{(r,cr)} = 0 \quad (1)$$

Similarly, for the control volume surrounding the entrained airstream (Fig. 2a extending around the rocket exhaust), one can write

$$\dot{m}_a u_{(a,i)} + p_{(a,i)} A_{(a,i)} - \dot{m}_a u_{(a,cr)} - p_{(a,cr)} A_{(a,cr)} - \int_{sl} p \, \mathrm{d}A = 0 \quad (2)$$

The subscripts represent the stream under consideration (for use in determining fluid properties such as the ratio of specific heats), followed by the location of interest. Expressing the term $(\dot{m}u + pA)$ as

$$\dot{m}u + pA = \dot{m}a\{M + (1/\gamma M)\} \quad (3)$$

whereas relating a to a^* locally, one obtains

$$\dot{m}u + pA = \dot{m}a^* \chi \quad (4)$$

where χ is defined as

$$\chi(\gamma, M) = \frac{M + (1/\gamma M)}{\sqrt{[2/(\gamma+1)] + [(\gamma-1)/(\gamma+1)]M^2}} \quad (5)$$

Summing Eqs. (1) and (2) while using Eq. (4) to simplify the result allows the streamwise momentum equation from station i to cr to be expressed as

$$\dot{m}_r a_r^* \{\chi_{(r,i)} - \chi_{(r,cr)}\} + \dot{m}_a a_a^* \{\chi_{(a,i)} - \chi_{(a,cr)}\} = 0 \quad (6)$$

Applying the principle of mass conservation to the two control volumes between the inlet and critical locations (while assuming that the ejector area remains constant) allows the following to be written:

$$\mu_{(a,i)} - \mu_{(a,cr)}\left(1 + [\sigma/(1-\sigma)]\left\{1 - \left[\mu_{(r,i)}/\mu_{(r,cr)}\right]\right\}\right) = 0 \quad (7)$$

where μ is defined as

$$\mu(\gamma, M) = \sqrt{\gamma} M \{1 + [(\gamma-1)/2]M^2\}^{-(\gamma+1)/[2(\gamma-1)]} \quad (8)$$

and σ represents the ratio of rocket exhaust to ejector inlet areas,

$$\sigma = A_{(r,i)} \big/ \left(A_{(r,i)} + A_{(a,i)}\right) \quad (9)$$

For most ejector designs, there are four key parameters that completely define the resulting flowfield. The first, σ, sets the overall ejector inlet geometry and has already been defined using Eq. (9). The second and third, θ and ζ, set the ratio between the air and rocket exhaust specific total enthalpies and total pressures, respectively,

$$\theta = \left(C_{p_a} T_a^0\right) \big/ \left(C_{p_r} T_r^0\right), \qquad \zeta = p_r^0 \big/ p_a^0 \quad (10)$$

whereas the fourth, α, represents the ratio of air to rocket exhaust mass flows. Note that the mass flow can be expressed using Eq. (8) as

$$\dot{m}/A = \left(p^0 \big/ \sqrt{RT^0}\right)\mu \quad (11)$$

which allows α to be written as a function of the other three ejector parameters as

$$\alpha = \frac{\dot{m}_a}{\dot{m}_r} = \left(\frac{1}{\zeta}\right)\left(\frac{1-\sigma}{\sigma}\right)\left(\frac{1}{\sqrt{\theta}}\right)\left[\frac{\gamma_a(\gamma_r - 1)}{\gamma_r(\gamma_a - 1)}\right]^{\frac{1}{2}} \frac{\mu_{(a,i)}}{\mu_{(r,i)}} \quad (12)$$

With these ejector variables defined, one can rewrite Eq. (6) as

$$\chi_{(a,i)} - \chi_{(a,cr)} + \left\{1 \big/ \left[\alpha\sqrt{\theta}\,\Gamma_{(a,r)}\right]\right\}\left[\chi_{(r,i)} - \chi_{(r,cr)}\right] = 0 \quad (13)$$

where

$$\Gamma_{(a,r)} = \sqrt{\frac{(\gamma_a - 1)(\gamma_r + 1)}{(\gamma_a + 1)(\gamma_r - 1)}} \quad (14)$$

If one assumes that the total conditions and the ejector inlet geometry are known (T_a^0, T_r^0, p_a^0, p_r^0, and σ), in addition to the gas composition of both the rocket and airstreams ($\gamma_a, \gamma_r, C_{p_a}$, and C_{p_r}), then there remain only four unknowns in Eqs. (7) and (13). These are the four Mach numbers required to solve for the various χ and μ values within both the air and rocket exhaust. However, assuming that the Mach number of the rocket exhaust entering the ejector $[M_{(r,i)}]$ is a known parameter, while recalling the assumption that the subsonic airstream reaches sonic velocity at the critical station $[M_{(a,cr)} = 1]$, one reduces the total number of unknowns to two, the air inflow Mach number at the ejector inlet $[M_{(a,i)}]$ and the rocket exhaust Mach number at the critical location $[M_{(r,cr)}]$. With only two unknowns, Eqs. (7) and (13) are sufficient to solve for the remaining ejector variables and, hence, define the resulting flowfield. Once the airflow Mach number at the ejector inlet is determined, the ejector inflow conditions are completely defined and can be used to calculate mixed flow exit properties. Assuming complete mixing between the two streams and applying the principle of energy conservation to the flow through the entire ejector (from stations i to e, Fig. 1), one obtains for the properties at the ejector exit plane

$$\begin{aligned} \mathcal{M}_e &= [1/(\alpha+1)](\alpha\mathcal{M}_a + \mathcal{M}_r) \\ \gamma_e &= [1/(\alpha+1)](\alpha\gamma_a + \gamma_r) \qquad (15) \\ C_{p_e} &= [\gamma_e/(\gamma_e - 1)](\bar{R}/\mathcal{M}_e) \end{aligned}$$

$$T_e^0 = 1/[C_{p_e}(\alpha+1)]\left(\alpha C_{p_a} T_a^0 + C_{p_r} T_r^0\right) \quad (16)$$

where, from the conservation of momentum, one obtains

$$\chi_e = 1 \big/ \left[a_e^*(\alpha+1)\right]\left(\alpha a_a^* \chi_{(a,i)} + a_r^* \chi_{(r,i)}\right) \quad (17)$$

Equation (17) yields two possible Mach numbers at the exit plane, relating to both a subsonic and a supersonic exit condition. As stated earlier, the assumption that the entrained airflow will choke within the upstream section of the ejector makes the supersonic solution the most likely outcome in the absence of specified exit conditions. With both the total temperature and Mach number at the exit plane, the total pressure of the mixed stream can be calculated using Eq. (11) and used to evaluate the compression ratio,

$$\pi_e = p_e^0 \big/ p_a^0 \tag{18}$$

Evaluating π_e as defined by Eq. (18) for the various ejector flowfield configurations considered hereafter, and comparing it to the value determined using the preceding theoretical analysis (which assumes complete mixing), one obtains a measure of effectiveness for a given ejector flowfield configuration.

Numerical Solution

The axisymmetric, multispecies, Favre averaged Navier–Stokes equations combined with the Wilcox k–ω turbulence model (including the Wilcox dilatational dissipation correction) are solved in generalized curvilinear form using WARP.[21,22] This code uses an implicit Euler time-marching scheme incorporating block implicit factorization to iterate toward a steady-state solution using a pseudotime step determined from a combination of both the minimum and maximum Courant–Friedrich–Levy number based local time-step conditions. The convective terms are treated using the Roe scheme in conjunction with Yee flux limiters, whereas the diffusive terms are treated with a second-order accurate, centered, finite differencing stencil. Convergence is judged against the magnitude of both the continuity and energy residuals. Details of the validation of this code on other nonaxisymmetric high-speed flows can be found in Ref. 23, whereas its application to axisymmetric flows has been tested in Ref. 24. In flux vector form, the governing equations can be expressed as

$$\frac{\partial \boldsymbol{Q}}{\partial t} + \frac{\partial \boldsymbol{E}}{\partial x} + \frac{\partial \boldsymbol{F}}{\partial r} + \boldsymbol{S}_{\text{axi}} - \boldsymbol{S}_{k-\omega} - \frac{\partial \boldsymbol{E}_v}{\partial x} - \frac{\partial \boldsymbol{F}_v}{\partial r} - \boldsymbol{S}_{\text{axi}_v} = 0 \tag{19}$$

The inviscid flux vectors are

$$\boldsymbol{Q} = \begin{bmatrix} \bar\rho\tilde c_1 \\ \vdots \\ \bar\rho\tilde c_k \\ \bar\rho\tilde u \\ \bar\rho\tilde v \\ \bar\rho\tilde E \\ \bar\rho k \\ \bar\rho\omega \end{bmatrix}, \qquad \boldsymbol{E} = \begin{bmatrix} \bar\rho\tilde c_1\tilde u \\ \vdots \\ \bar\rho\tilde c_k\tilde u \\ \bar\rho\tilde u^2 + p^* \\ \bar\rho\tilde u\tilde v \\ \tilde u(\bar\rho\tilde E + p^*) \\ \tilde u\bar\rho k \\ \tilde u\bar\rho\omega \end{bmatrix}, \qquad \boldsymbol{F} = \begin{bmatrix} \bar\rho\tilde c_1\tilde v \\ \vdots \\ \bar\rho\tilde c_k\tilde v \\ \bar\rho\tilde u\tilde v \\ \bar\rho\tilde v^2 + p^* \\ \tilde v(\bar\rho\tilde E + p^*) \\ \tilde v\bar\rho k \\ \tilde v\bar\rho\omega \end{bmatrix} \tag{20}$$

The viscous flux vectors are

$$\boldsymbol{E}_v = \begin{bmatrix} \nu_1^* \dfrac{\partial\tilde c_1}{\partial x} \\ \vdots \\ \nu_k^* \dfrac{\partial\tilde c_k}{\partial x} \\ \tilde\tau_{xx} \\ \tilde\tau_{xr} \\ \displaystyle\sum_k \left(\tilde h_k \nu_k^* \frac{\partial\tilde c_k}{\partial x}\right) + \kappa^* \frac{\partial\tilde T}{\partial x} + \tilde\tau_{xx}\tilde u + \tilde\tau_{xr}\tilde v + \mu_k^* \frac{\partial k}{\partial x} \\ \mu_k^* \dfrac{\partial k}{\partial x} \\ \mu_{\varepsilon_s}^* \dfrac{\partial\omega}{\partial x} \end{bmatrix}$$

$$\boldsymbol{F}_v = \begin{bmatrix} \nu_1^* \dfrac{\partial\tilde c_1}{\partial r} \\ \vdots \\ \nu_k^* \dfrac{\partial\tilde c_k}{\partial r} \\ \tilde\tau_{rx} \\ \tilde\tau_{rr} \\ \displaystyle\sum_k \left(\tilde h_k \nu_k^* \frac{\partial\tilde c_k}{\partial r}\right) + \kappa^* \frac{\partial\tilde T}{\partial r} + \tilde\tau_{rx}\tilde u + \tilde\tau_{rr}\tilde v + \mu_k^* \frac{\partial k}{\partial r} \\ \mu_k^* \dfrac{\partial k}{\partial r} \\ \mu_{\varepsilon_s}^* \dfrac{\partial\omega}{\partial r} \end{bmatrix} \tag{21}$$

and the remaining vectors are written

$$\boldsymbol{S}_{\text{axi}} = \frac{1}{r}\begin{bmatrix} \bar\rho\tilde c_1\tilde v \\ \vdots \\ \bar\rho\tilde c_k\tilde v \\ \bar\rho\tilde u\tilde v \\ \bar\rho\tilde v^2 \\ \tilde v(\bar\rho\tilde E + p^*) \\ \tilde v\bar\rho k \\ \tilde v\bar\rho\omega \end{bmatrix}, \qquad \boldsymbol{S}_{k-\omega} = \begin{bmatrix} 0 \\ \vdots \\ 0 \\ 0 \\ 0 \\ 0 \\ S_k \\ S_\omega \end{bmatrix} \tag{22}$$

$$\boldsymbol{S}_{\text{axi}_v} = \frac{1}{r} \times \begin{bmatrix} \nu_1^* \dfrac{\partial\tilde c_1}{\partial r} \\ \vdots \\ \nu_k^* \dfrac{\partial\tilde c_k}{\partial r} \\ \tilde\tau_{rx} - r\dfrac{2}{3}\dfrac{\partial}{\partial x}\left(\mu^*\dfrac{\tilde v}{r}\right) \\ \tilde\tau_{rr} - \tilde\tau_{\theta\theta} - \dfrac{2}{3}\mu^*\dfrac{\tilde v}{r} - r\dfrac{2}{3}\dfrac{\partial}{\partial r}\left(\mu^*\dfrac{\tilde v}{r}\right) \\ \left(\begin{aligned} &\sum_k \left(\tilde h_k \nu_k^* \frac{\partial\tilde c_k}{\partial r}\right) + \kappa^* \frac{\partial\tilde T}{\partial r} + \tilde\tau_{rx}\tilde u + \tilde\tau_{rr}\tilde v + \mu_k^* \frac{\partial k}{\partial r} \\ &\quad + \mu_k^* \frac{\partial k}{\partial r} - \frac{2}{3}\mu^*\frac{\tilde v^2}{r} - r\frac{2}{3}\frac{\partial}{\partial x}\left(\mu^*\frac{\tilde u\tilde v}{r}\right) - r\frac{2}{3}\frac{\partial}{\partial r}\left(\mu^*\frac{\tilde v^2}{r}\right) \end{aligned}\right) \\ \boldsymbol{S}_{\text{axi}_v} \\ \mu_{\varepsilon_s}^* \dfrac{\partial\omega}{\partial r} \end{bmatrix} \tag{23}$$

Both the pressure and energy terms contain turbulent effects through the inclusion of the specific turbulent kinetic energy k,

$$p^* = \bar p + \tfrac{2}{3}\bar\rho k, \qquad \tilde E = \tilde e + k + \tfrac{1}{2}(\tilde u^2 + \tilde v^2) \tag{24}$$

In all cases, viscosity, thermal conductivity, and diffusion include the effect of turbulence through the definition of modified coefficients,

$$\mu^* = \bar\mu + \mu_T \tag{25}$$

where

$$\mu_T = (9/100)\bar\rho(k/\omega)$$

The source term for the turbulent kinetic energy equation is given by

$$\boldsymbol{S}_k = P_k - \bar\rho(k \times \omega + \varepsilon_d) \tag{26}$$

where the production term is written

$$P_k = \left(\tau^{\dagger}_{xx} - \frac{2}{3}\bar{\rho}k\right)\frac{\partial \tilde{u}}{\partial x} + \tau^{\dagger}_{xr}\left(\frac{\partial \tilde{u}}{\partial r} + \frac{\partial \tilde{v}}{\partial x}\right) + \left(\tau^{\dagger}_{rr} - \frac{2}{3}\bar{\rho}k\right)\frac{\partial \tilde{v}}{\partial r}$$
$$- \mu_T \frac{2}{3}\frac{\tilde{v}}{r}\left(\frac{\partial \tilde{u}}{\partial x} + \frac{\partial \tilde{v}}{\partial r}\right) \tag{27}$$

The dilatational dissipation correction by Wilcox,[25] ε_d, is calculated using

$$\varepsilon_d = (3/2)k \times \omega\{\max[(2k/a^2) - (1/16), 0]\} \tag{28}$$

which is also used in the specific dissipation rate equation source term

$$S_\omega = (\omega/k)\big\{(C_{\varepsilon_1} - 1)P_k - (C_{\varepsilon_2} - 1)\bar{\rho}k \times \omega + \bar{\rho}\varepsilon_d\big\} \tag{29}$$

Code Validation

WARP's ability to simulate accurately the coflowing streams of dramatically different properties that occur within an ejector is tested against data from Goebel and Dutton[26] for a turbulent subsonic/supersonic shear layer. Two cases in particular are examined, the difference between the two being the degree of compressibility of each mixing layer. At the lower convective Mach number, Cottrell and Plesniak[27] showed that an incompressible code can accurately capture the flowfield dynamics of the subsonic/supersonic shear layer. However, they found poor agreement between numerical and experimental results at convective Mach numbers higher than approximately 0.7, which they partially attributed to a lack of sufficient compressibility modeling.

In each case presented here, the same gridding and turbulence parameters are used: a two-dimensional grid of dimensions 250 × 150 containing clustering near the end of the splitter plate and along all surfaces. The turbulent Schmidt number is set to unity, the turbulent Prandtl number is set to 0.5 (the value recommended for free shear flows[28]), and the freestream value of ω is set to 10 times the flow speed. The inflow boundary is split above and below the splitter plate, with the upper-half specified as supersonic inflow (constant Mach number, pressure, and temperature) and the lower-half as subsonic inflow (constant total pressure and total temperature). All splitter plate surfaces are specified as no slip, whereas the upper and lower walls are specified as inviscid to avoid any boundary-layer/shear-layer interaction. The outflow is split similar to the inflow, with the upper-half using a supersonic exit condition and the lower-half requiring a specified static pressure (set to obtain matched inflow conditions with the experimental data, Table 1). The numerical computations are considered converged when the residual has been reduced by approximately seven orders of magnitude.

In the work of Goebel and Dutton, the test cases are listed by their relative Mach numbers M_{rel}, defined as

$$M_{\text{rel}} \equiv \frac{u_1 - u_2}{\frac{1}{2}(a_1 + a_2)} \tag{30}$$

where u is the local mean streamwise velocity and a is the speed of sound. (The subscripts differentiate between the supersonic and subsonic streams.) The authors prefer this value over the more conventional convective Mach number, defined as

$$M_{1c} \equiv (U_c - u_1)/a_1 \qquad \text{or} \qquad M_{2c} = (u_2 - U_c)/a_2 \tag{31}$$

Table 1 Conditions at beginning of shear layer/end of splitter plate for both low and high relative Mach numbers

Variable	WARP	Goebel and Dutton[26]	WARP	Goebel and Dutton[26]
p_1/p_2, kPa	54/53	53/53	29/30	32/32
T_1/T_2, K	282/169	281/161	277/331	292/332
ρ_1/ρ_2, kg/m^3	0.66/1.09	0.66/1.15	0.37/0.31	0.38/0.34
δ_1/δ_2, mm	3.3/3.1	3.0/3.1	1.0/2.0	1.3/1.7
M_{rel}	1.19	1.37	1.84	1.97

where U_c is the convective velocity

$$U_c \equiv \frac{a_1 u_2 + a_2 u_1}{a_1 + a_2} \tag{32}$$

However, for streams with equal ratios of specific heats (as is the case in the experimental data) the relative Mach number is equal to one-half of the convective Mach number, and, thus, either can be used. For consistency with the experimental data, the relative Mach number will be quoted here, where a value of two replaces the convective Mach number of approximately one in terms of defining the boundary between incompressible and compressible shear layers.

Because the inflow boundary conditions for a subsonic stream cannot be completely fixed, matching the experimental conditions at the beginning of the shear layer, that is, the end of the splitter plate, becomes a nontrivial task. In addition, shear layer development is sensitive to the thickness of the boundary layers at its root (those developed along the upper and lower surfaces of the splitter plate), thus adding to the difficulty in matching the experimental conditions. For the cases shown here, it is found that a splitter plate length of 75 and 20 mm for the low and high relative Mach number cases, respectively, produces boundary layers in both the subsonic and supersonic streams that match those present in the experimental data (Table 1). The largest differences between the numerical and experimental data occur in the subsonic velocity at the end of the splitter plate, resulting in a 13% and 6% decrease in the computed relative Mach number for the low and high M_r cases, respectively. However, all other parameters match quite well, including the static pressures, which are key in preventing any unwanted deflection of the shear layer.

Figure 3 shows a comparison of both the streamwise velocity and specific turbulence kinetic energy profiles for the two cases considered. In Fig. 3a, despite the overprediction of the subsonic velocity, the velocity deficit seen in the experimental data caused by the boundary layer on the lower surface of the splitter plate is also predicted by the numerical results. As the downstream distance is increased to approximately 75 mm, both the lower edge of the shear layer and the subsonic velocity profile within the lower portion of the shear layer are captured quite well by the numerical results. However, past this point, the numerical results predict a more linear velocity profile than the experimental data. This is a result of the higher levels of turbulence predicted in the subsonic portion of the shear layer by the numerical simulation. By examining Fig. 3c, one can see that up to the 75-mm station the k profiles below the splitter plate match reasonably well. Past this point, the numerical profile appears fuller than the experimental data, suggesting a more turbulent flow and, thus, resulting in a more linear velocity profile. This affects the predicted lower boundary-layer edge, where the largest error occurs at the 150-mm location, at which point the numerically placed edge is approximately 60% lower than the experimentally determined value of 8.2 mm.

The results for the supersonic portion of the shear layer are quite different, with both the upper edge of the shear layer and velocity profile within the region above the splitter plate matching very well at all locations. As shown in Fig. 3a, except at the very first station (10 mm), the numerical velocity follows the experimental data nearly perfectly, with the numerical boundary-layer edge differing by no more than 20% from that determined from the experimental data. Qualitatively, the same is true for the turbulence results, with the data within the supersonic portion of the shear layer matching better than in the subsonic portion. When the peak turbulence values in Fig. 3c are examined at each location, the vertical position of the maximum turbulence kinetic energy appears to match the experimental data reasonably well. Although there does not appear to be an experimental data point at the peak turbulence position at each station, the numerically predicted maximum value of k is within 25% of the experimental value at all stations, a difference that decreases with increasing distance from the splitter plate.

Figure 3b shows the streamwise velocity profiles for the higher convective Mach number case, where, when these results are compared to those in Fig. 3a, it appears that the computational technique handles the higher relative Mach number case better. This is due in

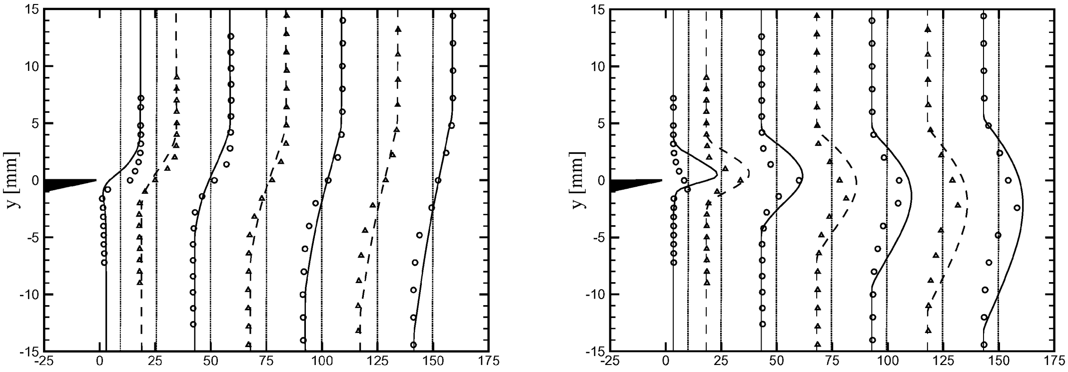

a) $M_{\mathrm{rel}} = 1.37$**, streamwise velocity values 0–500 m/s**

c) $M_{\mathrm{rel}} = 1.37$**, turbulence kinetic energy values 0–5000** $\mathbf{m^2/s^2}$

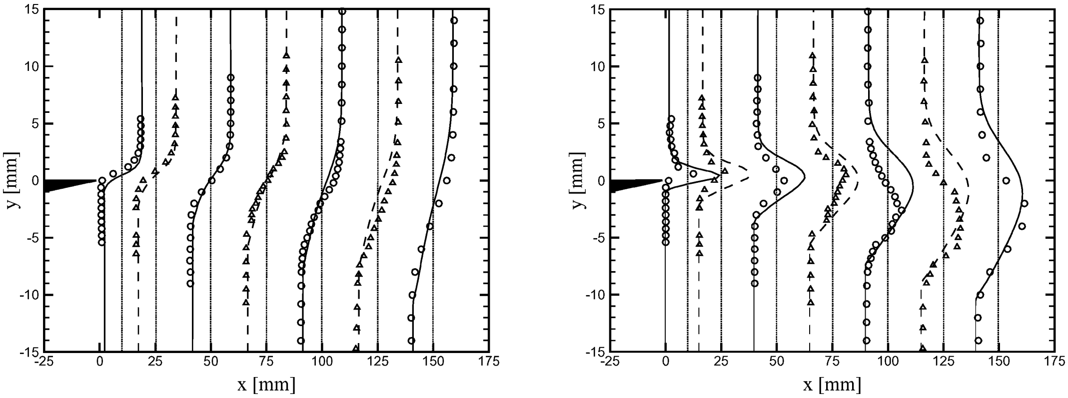

b) $M_{\mathrm{rel}} = 1.97$**, streamwise velocity values 0–1000 m/s**

d) $M_{\mathrm{rel}} = 1.97$**, turbulence kinetic energy values 0–15,000** $\mathbf{m^2/s^2}$

Fig. 3 Comparison of WARP results (——, - - - -) with data from Goebel and Dutton[26] (○ ○ ○, △△△) for $M_{\mathrm{rel}} = 1.37$ **and** $M_{\mathrm{rel}} = 1.97$**.**

large part to the experimental data within the subsonic portion of the shear layer being more linear, a trend more consistent with the numerical results. This is also consistent with the absolute magnitude of the turbulence in the $M_{\mathrm{rel}} = 1.97$ case being approximately three times that seen in the $M_{\mathrm{rel}} = 1.37$ case (15,000 m^2/s^2 compared to 5000 m^2/s^2). Although the overprediction of the subsonic velocity remains evident throughout the numerical results, this has little effect on either of the boundary-layer edges because in most cases the numerical and experimental values are within approximately 30% of each other. The exceptions to this are at the 100- and 125-mm locations, where the upper edge of the shear layer is overpredicted by approximately 60%.

This increased discrepancy also coincides with the locations where the largest differences between the numerical and experimental k profiles occur (Fig. 3d, 100 and 125 mm). At these two locations the experimental peak in k deflects significantly below the splitter plate (to approximately 4 mm), whereas the numerical peak remains consistently near the height of the splitter plate along the entire length of the duct. However, at the final station (150 mm) the experimental peak returns to a more central value, thereby restoring the agreement between the numerical and experimental profiles.

Although the magnitude of the maximum value of k is overpredicted by the numerical results at nearly all of the locations in Fig. 3d, this overprediction is reduced from 94% immediately downstream of the splitter plate to 22% at the 125-mm location and becomes an underprediction of approximately 4% at the 150-mm station.

Ejector Flowfield Simulations

For the ejector section of an RBCC engine to be effective, the flow at its exit plane must have a total pressure as high as possible compared to that of the entrained air, while also providing adequate mixing. The simplest configuration, shown in Fig. 4a, is to have a single rocket placed along the axis of symmetry. Another is to have the rocket exhaust distributed within the ejector inflow

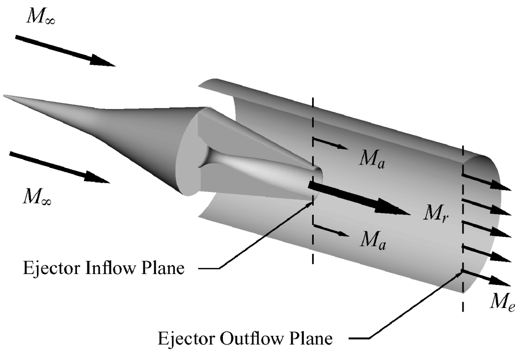

a) Central configuration

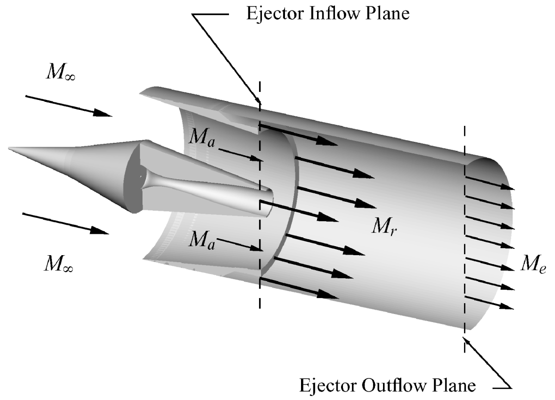

b) Central/annular configuration

Fig. 4 Rocket placement within ejector section of RBCC engine.

plane as shown in Fig. 4b, where an annular rocket is added along the outer diameter of the ejector duct in an effort to improve ejector performance. The second configuration also has the benefit of being capable of altering the distribution of rocket exhaust mass flow between the two rocket streams to achieve optimum levels of performance.

For all of the cases shown, both the total pressure and total temperature are held constant at the air inflow boundary, thus allowing the inflow Mach number to change, which in turn leaves the air mass flow rate free to adjust to the ejector flowfield. The rocket exhaust inflow boundary is supersonic with the Mach number, static pressure, and static temperature specified. The outer wall of the ejector, as well as the 10 mm sections of rocket wall protruding into the ejector section, are specified as no-slip, adiabatic walls, whereas the central axis boundary is symmetric. To avoid dividing by zero near the axisymmetric axis, an offset of 0.01 μm is applied along the length of the ejector. Unless stated otherwise, the outflow boundary is specified as supersonic. (It is assumed that the entrained airflow chokes during the initial section of the ejector and that the resulting mixed flow remains supersonic.) The turbulent Schmidt and Prandtl numbers are set to 1.0 and 0.5, respectively, whereas the freestream value of ω is set to 10 times the flow speed (with the wall value set to the value recommended by Wilcox[28]). The flowfields in all cases are judged converged when the residual has been reduced by approximately eight orders of magnitude.

Central Rocket Configuration

The simplest ejector configuration, that with a single central rocket located along the axisymmetric axis of the ejector section, is examined using the conditions listed in Table 2. On a molar basis, the air is modeled as 80% N_2 and 20% O_2, whereas the rocket exhaust is composed of 76% O_2, 17% CO_2, and 7% H_2O. This corresponds to the equilibrium post combustion mixture for kerosene and oxygen at an equivalence ratio of 0.2 based on the reaction

$$\phi C_{12}H_{24} + 18O_2 \longrightarrow 12H_2O + 12CO_2 \qquad (33)$$

The equivalence ratio is chosen such that no combustible species enter the ejector, thus, eliminating the possibility of simultaneous mixing and combustion. Although this is not typical of RBCC operating conditions, it is expected that the primary effect of increased equivalence ratios would be in promoting combustion within the ejector, not increasing the rate at which the two streams mix (which is the focus of the present work).

In an effort to evaluate the mixing potential of this configuration, three different rocket exhaust Mach numbers are examined, 3.00, 2.50, and 2.25. This is done to increase the static pressure at the rocket exit plane, thereby changing the manner in which the exhaust stream impinges on the incoming air. Because a larger pressure differential between the rocket exhaust and airstreams will cause the shear layer to deflect radially outward the resulting surface area between the two streams will increase and, thus, enhance the potential for increased mixing. The upper limit on the exhaust Mach number is chosen such that there are no cases where the rocket static pressure is less than that of the air, thereby ensuring that the rocket exhaust always expands into the airflow. Although both θ and ζ remain constant between the cases considered due to their dependence on the total conditions within the ejector, to keep σ constant the rocket throat height must be varied to accommodate the different expansion ratios required to produce the desired M_r. This in turn changes the rocket exhaust mass flow and, thus, α, as shown in Table 3. This change in α is also affected by the expansion of the rocket exhaust because a larger expansion creates a smaller airflow choke area (Fig. 2).

Table 2 Rocket exhaust and ejector parameters for the configurations shown in Fig. 4

Configuration	Central	Central/annular
Altitude, m	6300 (20,669 ft)	6300 (20,669 ft)
M_∞	2.0	0.8
p_a^0, kPa	301 (3 atm)	58.7 (0.58 atm)
T_a^0, K	445	267
p_a^0/p_∞^0	0.85	0.85
p_r^0, MPa	15.2 (150 atm)	5.87 (58 atm)
T_r^0, K	2322	2316
ϕ	0.2	0.2
γ	1.238	1.275
σ	0.05	0.10
θ	0.14	0.09
ζ	50	100

Table 3 Comparison of ejector performance for various rocket exhaust Mach numbers

Variable	$M_r = 3.00$	$M_r = 2.50$	$M_r = 2.25$
p_r/p_a	1.61	3.38	4.93
$\dot{m}_r$, kg/s	3.07	5.88	7.98
$M_{(a,i)}$	0.72	0.52	0.42
α	5.16	2.25	1.41

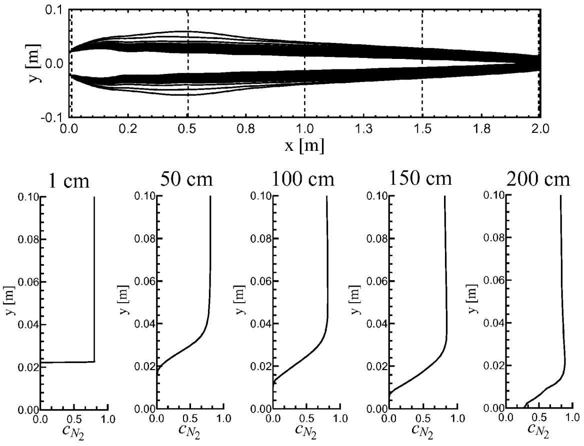

a) $M_r = 3.00$

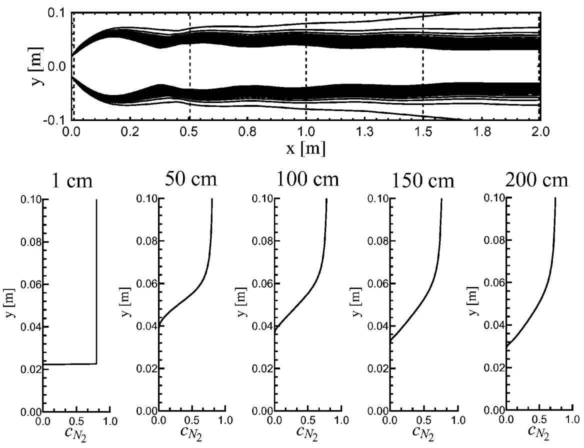

b) $M_r = 2.25$

Fig. 5 Nitrogen mass fraction profiles for central configuration.

Figure 5 shows the nitrogen mass fraction contours within the ejector for both the $M_r = 3.00$ and 2.25 cases. Note that the resulting flowfield is similar to that assumed to occur when treating a theoretical one-dimensional ejector (Fig. 2a). In both cases, the incoming airflow reaches the critical minimum area location in less than 20 cm, whereas the Mach number at the exit plane is sonic or higher in each case considered. As shown in Table 3, the major difference between the cases is the entrained air Mach number at the ejector inflow ($M_{(a,i)}$), where, for $M_r = 3.00$, it is approximately 70% higher than when $M_r = 2.25$. This is due to the lesser degree of contraction experienced by the airflow in the higher exhaust Mach number case (where the static pressures are nearly matched), requiring a higher incoming Mach number if the subsonic flow is to choke. This is consistent with the air inflow boundary being specified as constant total temperature and pressure, thus allowing the inflow Mach number to vary.

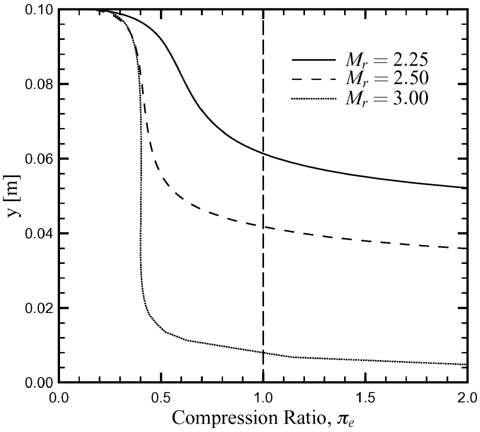

Fig. 6 Compression ratio across upper-half of exit plane of 2.0-m ejector as shown in Fig. 4a.

In addition to the detrimental effect on α of a lower air inflow Mach number, the larger throat area required for the $M_r = 2.25$ case (recalling that σ is held constant) translates into a higher rocket exhaust mass flow rate $\dot{m}_r$. These two factors contribute to decrease α by a factor of four, from 5.16 in the $M_r = 3.00$ case to near unity (1.41) when the exhaust Mach number is lowered to 2.25. Because one of the main benefits of an RBCC engine is its use of atmospheric air, one must be careful when reducing α. Although this tends to increase the resulting compression ratio [Eq. (18)], it also has the undesirable effect of making the engine behave more like a pure rocket than an airbreathing engine, especially when the rocket mass flow significantly outweighs that of the entrained air ($\alpha \ll 1$).

The clear segregation of the two flow streams, even in the case with a large degree of rocket exhaust expansion, prevents any significant transfer of momentum and energy to the entrained air. As shown in Fig. 6, the total pressure of the airstream is actually decreased over the length of the ejector ($\pi_e < 1$), where decreasing M_r acts only to increase the size of the unmixed rocket exhaust region at the exit plane (as shown by the region of π_e off of the scale in Fig. 6). Although on a mass flow averaged basis the $M_r = 2.25$ case produces a π_e greater than unity, this neglects that the flow is not truly mixed and includes a significant region of unmixed rocket exhaust (below radii of approximately 6 cm). As Fig. 6 shows, if one calculates π_e based on the airflow regions alone, the result is quite different, showing in fact that the ejector actually decreases, as opposed to increasing, the total pressure in these regions. Therefore, by virtue of the poor mixing qualities of this configuration, independent of the degree to which the rocket exhaust expands into the airflow, it can be concluded that a more sophisticated rocket exhaust geometry must be employed to achieve adequate levels of ejector performance.

Annular/Central Rocket Configuration

To produce an ejector with improved levels of performance, the configuration shown in Fig. 4b is examined using annular rockets injecting one-half and three-quarters of the total rocket exhaust mass flow into the ejector. In these cases the rocket chamber combustion pressure is lowered to 58 atm to reflect a smaller-size rocket more suited for use in a multiple-rocket configuration. Because a change in p_r^0 will affect ζ, which in turn will affect other ejector variables such as α [Eq. (12)], the one-dimensional ejector theory can be used to ensure that the resulting operating conditions are capable of producing suitable levels of performance. Fixing the rocket exhaust Mach number $M_r = M_{(r,i)}$ at 3.10 yields a static pressure ratio of approximately two between the rocket exhaust and airstreams, if one reduces the freestream Mach number to 0.8 at the same altitude. The rocket exhaust area is also increased to keep the total rocket exhaust mass flow near the value obtained in the $M_r = 3.00$ central configuration case, which, for a constant area ejector, results in an increased value for σ. These changes are reflected in Table 2, whereas the theoretical performance of a one-dimensional ejector at these conditions is shown in Table 4.

Table 4 Ejector exit properties for various annular rocket sizes

Variable	$75_A/25_C$	$50_A/50_C$	$0_A/100_C$	One-dimensional theory
α	1.00	0.98	1.09	1.45
M_e	1.30	1.36	1.99	1.49
π_e[a]	2.47	1.97	1.36	2.88

[a] Mass flow averaged over mixed exit flow only, see Fig. 8.

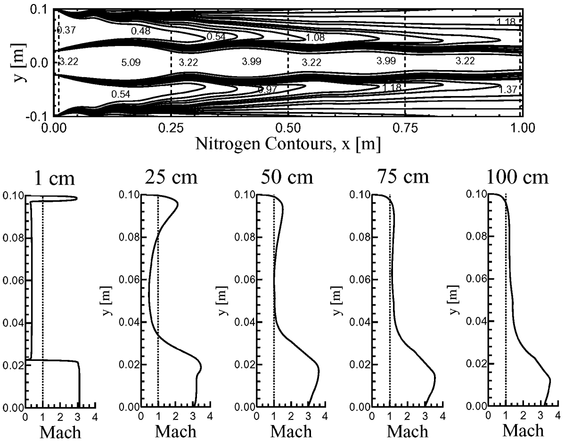

a) $50_A/50_C$

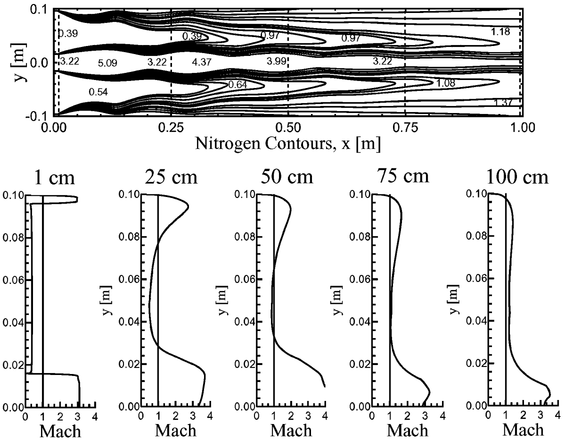

b) $75_A/25_C$

Fig. 7 Nitrogen mass fraction contours and Mach number profiles for annular/central configurations.

Figure 7 shows the nitrogen contours (with Mach numbers overlayed) for both annular/central configurations in addition to the Mach number profiles at various locations within the ejector. In comparison to the preceding results, one of the most striking differences is the location at which the entrained air reaches the critical location. Whereas the airflow in the single central rocket configuration reaches a minimum area within approximately 20 cm, the presence of an annular rocket stream more than doubles this distance. Comparing Figs. 5 and 7, one can see that the annular rocket stream undergoes several expansion/compression cycles during the same distance that the central rocket stream undergoes a single cycle. This increases the degree to which the annular rocket exhaust and airstreams mix, to the point that by the time the entrained air reaches sonic velocity, one can no longer reasonably assume a zero thickness shear layer between the two streams (because there is no longer a distinct annular rocket stream). This results in a lower value for α as compared to the theoretical ejector, where a value of unity is approximately 30% lower than predicted (Table 4). At the exit plane, the $50_A/50_C$ configuration yields a slightly larger pure rocket core region than the $75_A/25_C$ configuration, resulting in a slightly higher mass flow averaged Mach number. However, this also results in the $75_A/25_C$ configuration having the most uniform

Mach number profile over the largest area, with a greater quantity of the exit flow at the mixed flow Mach number. Therefore, in terms of effectively mixing the rocket and airstreams, the annular/central configuration results in very acceptable levels of performance, with the $75_A/25_C$ configuration yielding the most uniform exit flow.

In terms of the evaluation of the compression ratio, the presence of a pure rocket core along the axisymmetric axis can bias the results toward configurations with larger cores as the exhaust total pressure starts 100 times that of the incoming air. Therefore, to determine the radius below which one will consider the flow unmixed and, thus, neglect it when calculating the total pressure, the method in Fig. 8 is used. First, one evaluates the average streamwise velocity within the mixed flow region in one of the three following ways: 1) For profiles in which there are still two discernible higher velocity regions due to the two exhaust streams, the lowest velocity between these two regions is taken as the average mixed flow velocity (Fig. 8a); 2) In cases where the annular rocket stream is no longer visible in the velocity profile, the largest uniform velocity region above the central rocket stream is taken as the average mixed flow velocity (Fig. 8b); 3) For the remaining cases, where there is neither a uniform velocity region nor a visible annular exhaust stream, the inflection point at the largest radius outside of the boundary layer is taken as the average mixed flow velocity (Fig. 8c). Because the minimum velocity of the exit flow is zero (due to the boundary layer along the inner wall of the ejector duct), making the mixed flow maximum velocity twice the average velocity results in an average that lies at the median position of the resulting mixed flow velocity profile. Given that the highest streamwise velocities occur along the axis at the center of the rocket core, as the radial distance increases, the streamwise velocity decreases until it reaches this threshold maximum value ($2u_{\text{ave}}$). The total pressure is then calculated on a mass flow averaged basis from this radial position outward, thereby avoiding any artificial inflation of the compression ratio. As a consequence, for ejector configurations where the mixing is poor, a greater portion of the exit area is neglected, as shown by the hatched regions in Fig. 8.

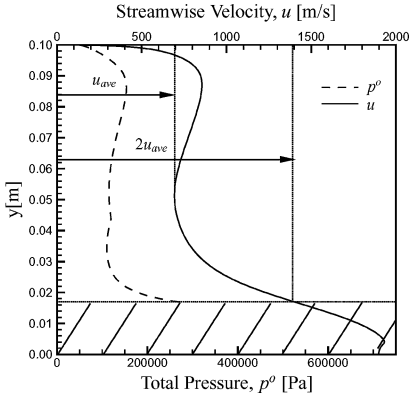

a) $75_A/25_C$

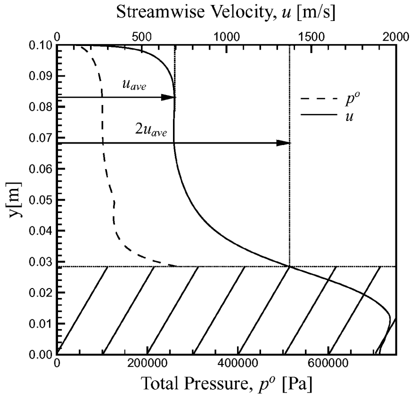

b) $50_A/50_C$

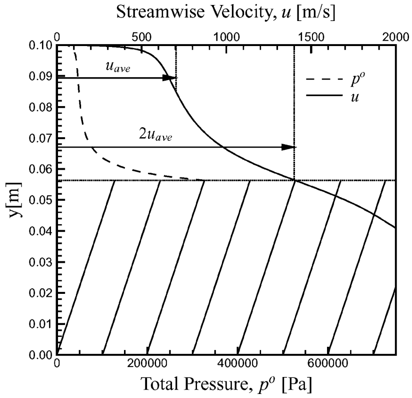

c) $0_A/100_C$

Fig. 8 Determination of lower radial bound of mixed flow region (for use in calculating π_e).

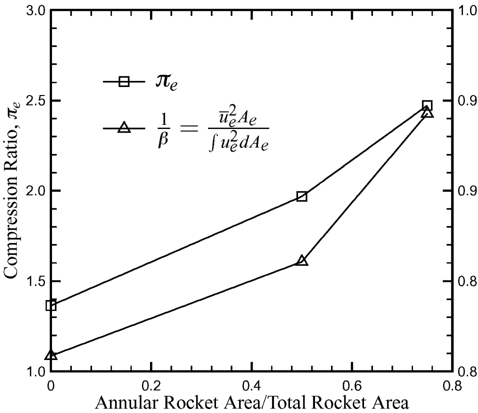

Fig. 9 Ejector performance for various annular rocket sizes.

Defining the mixed flow regions as shown in Fig. 8 produces the compression ratios shown in Fig. 9. Note that, not only does the $75_A/25_C$ case produce the compression ratio highest in absolute magnitude (≈ 2.5), it also produces the most uniform profile at the 1.0-m location. This uniformity is quantified by the parameter β, where the inverse of this quantity reaches unity for a perfectly flat velocity profile. As the annular rocket area is increased, $1/\beta$ increases, reflecting the diminishing size of the rocket core along the axis.

Indicative of the effectiveness of the annular rocket to impart its energy to the entrained airstream, the $75_A/25_C$ results not only show the largest compression ratio, but the value of 2.47 is only 14% below the theoretical compression ratio (which assumes complete mixing). As the annular rocket area decreases, so does the resulting compression ratio, with the single central rocket configuration showing the worst compression at the exit plane. It should also be noted that the compression ratio of the $75_A/25_C$ configuration is based on the largest percentage of the exit area at 95%, compared to 91% and 70% for the $50_A/50_C$ and $0_A/100_C$ cases, respectively.

Grid Convergence Analysis

All of the results presented for the 1.0-m ejectors are obtained on grids with dimensions of approximately 500 × 150, with slight variations in the distribution of the radial points to accommodate the different sizes of annular rockets. However, to assess the nature and degree of any grid induced error, the $75_A/25_C$ configuration is also simulated on a grid 4 times (1035 × 300) and 11 times (2000 × 450) denser than the base grid, resulting in a maximum grid density of nearly 1 million nodes.

Figure 10a shows the compression ratio profile across the upper-half of the ejector, 10 cm downstream of the inflow plane. Note that, although there is a noticeable difference in the annular rocket stream between the solution obtained using the coarse and medium size grids, both the medium and fine grids appear to produce nearly identical results. The approximately 20% underprediction by the

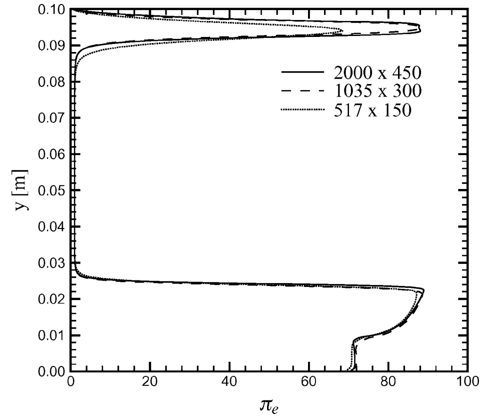

a) Compression ratio

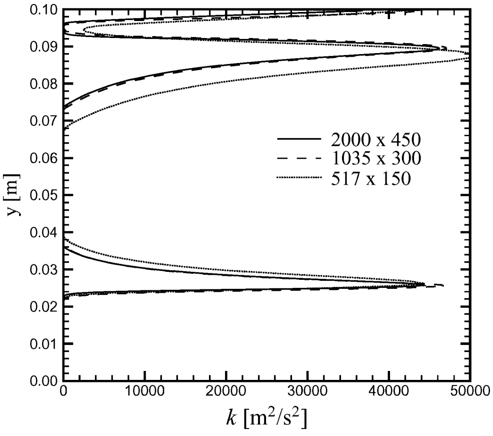

b) Turbulence

Fig. 10 Compression ratio and turbulence profiles for $75_A/25_C$ ejector configuration 10 cm from ejector inflow plane.

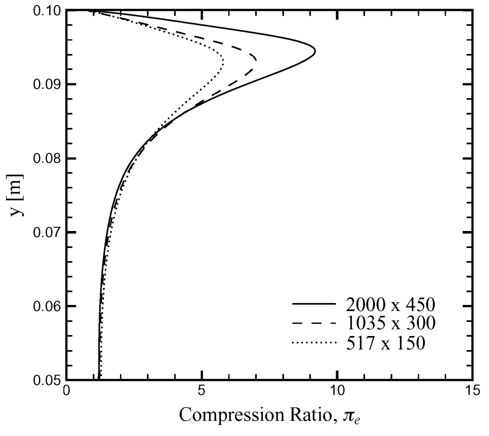

a) 50 cm

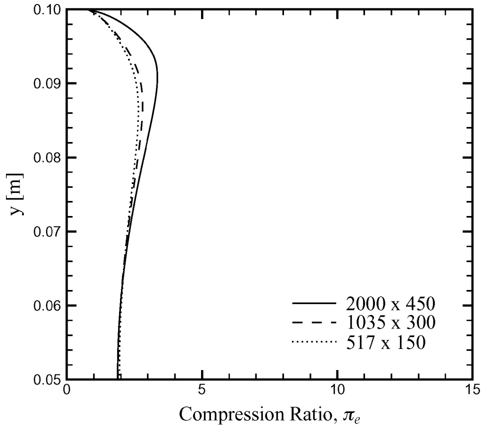

b) 100 cm

Fig. 11 Compression ratio profiles near annular exhaust stream for $75_A/25_C$ ejector configuration at ejector midpoint and exit.

coarse grid in the peak total pressure within the annular stream is due to the increased spread rate of the shear layer, best shown by the specific turbulence kinetic energy profiles in Fig. 10b. Note here that the coarse grid shifts the location of both the peak turbulence energy and the lower edge of the shear layer, approximately 4 cm toward the axis as compared to the medium and fine grid solutions. This more rapid spreading leads to a thicker shear layer with an increased level of turbulence, acting to decrease the peak total pressure within the annular rocket flow. Applying a Richardson extrapolation (see Ref. 29) to the data for the peak turbulence shown in Fig. 10b yields an error for the coarse grid of approximately 10%, whereas that of the fine grid is less than 1%. Thus, neglecting for the moment the effect the increased shear layer spreading has on the flowfield properties farther downstream, as judged by the properties at the 10-cm location, the fine grid appears to produce grid-converged results.

Comparing the compression ratio profiles in the annular exhaust region at both the midpoint and exit of the ejector (Figs. 11a and 11b), one observes that as the downstream distance is increased, the difference between the medium and fine grid solutions grows larger from the 10- to 50-cm locations, whereas farther downstream the solutions between these grids reapproach one another. As already observed from the conditions near the inflow plane, using a coarser grid increases the spread rate of the annular rocket stream. Thus, the farther downstream the ejector one travels, the greater the difference one expects in the size of the predicted shear layers (which would explain any differences observed between the coarse and finer grids). However, having observed that the solutions between the medium and fine grids are nearly identical at the 10-cm location, the increased differences between these grids farther downstream is indicative of the difficulty in accurately simulating the spread rate of the annular shear layer. This discrepancy suggests that although the grid density is sufficient in the radial direction using the medium grid, the same cannot be concluded about the streamwise direction, where the solution accuracy is affected by the manner in which the turbulent shear layer is propagated downstream. Because the gridding in the radial direction is constant from the 10-cm location to the ejector exit for both the medium and fine grids, any decreased accuracy must be due to either the grid density in the streamwise direction or the turbulence model itself. Because a grid finer than the largest used here would require in excess of 3.5 million nodes, the task of quantifying the error due to the grid spacing alone requires resources outside the reach of the present study. In addition, Wilcox[28] and Barber et al.[30] have noted that most turbulence models overpredict the rate at which an axisymmetric shear layer will spread. This effect is often referred to as the "round jet/plane jet" anomaly. Therefore, even in the absence of any differences between grids of consecutively larger dimensions, the distances at which any results are obtained are most likely optimistic due to the limitations of the turbulence model employed.

However, despite this uncertainty in the spread rate of the annular shear layer, at the exit plane the coarse and medium grid solutions match nearly perfectly. The mass flow averaged compression ratios differ by less than 3% and 10% between the coarse and medium grids and the coarse and fine grids, respectively (where the values obtained from the coarse grid are less than those found using the finer grids). Additionally, the differences between the medium and fine grids are smaller at the exit plane as compared to those at the ejector midpoint. This suggests that although the distances at which the profiles are taken depend on a coupling of the streamwise grid density and the turbulence model employed, the final profile is independent of these errors. As shown in Fig. 11b, both the coarse and medium grids predict approximately the same profile at the ejector exit, whereas the fine grid appears to be heading toward the same solution but at a slower pace (due to the reduction of the grid induced diffusion achieved through a refinement of the streamwise grid density).

Therefore, it is concluded that the coarse grid is sufficient in terms of accuracy to be used for simulating the ejector flowfield on the basis of the following results:

1) The limitations of the turbulence model employed restrict the degree to which an increased streamwise grid density will yield more accurate ejector lengths.

2) The exit flow profiles obtained using the finer grids tend to those obtained using the coarse grid only over increased distances.

3) The overall compression ratio at the exit plane as found using the coarse grid is within approximately 10% of that found using the finest grid (erring on the conservative side).

Summary

It is shown that an axisymmetric ejector configuration using only a single rocket located along the central axis (typically used for theoretical considerations) performs poorly. Even after lengths of 10 times the diameter of the ejector inlet, this configuration produces only marginally mixed flow at the exit while actually decreasing the total pressure when compared to that within the incoming airflow. Changing the degree to which the rocket exhaust expands into the airflow does little to improve the mixing. In fact, the effect is to decrease performance when evaluated against the amount of air the ejector is capable of ingesting.

The use of an ejector configuration that has 75% of the rocket exhaust enter the ejector through an annular stream along the outer wall dramatically increases both the rapidity of the mixing process within the ejector and the degree of mixing obtained at the exit. In this case, a compression ratio within 14% of the value obtained from a one-dimensional theoretical analysis assuming complete mixing is obtained. For the given flight and rocket conditions, this translates into a mixed flow extending across 95% of the total exit area with a total pressure nearly two and one-half times that of the entrained air when both the air and rocket exhaust mass flows are equal. These results also indicate that it is the annular rocket stream that mixes best with the entrained air, where only the central rocket stream is still identifiable at the exit. Given the inability of the central rocket exhaust to mix effectively with the rest of the flow, coupled with the annular rocket's nearly complete mixing, suggests the elimination of a central rocket altogether.

Acknowledgments

This work was sponsored by the Natural Science and Engineering Research Council of Canada. Thanks are also extended to Craig Dutton for providing the experimental data presented in this work.

References

[1] von Kármán, T., "Theoretical Remarks on Thrust Augmentation," *Reissner Anniversary Volume: Contributions to Applied Mechanics*, edited by P. I. of Brooklyn, J. W. Edwards, Ann Arbor, MI, 1949, pp. 461–468.

[2] Alperin, M., and Wu, J., "Recent Development of a Jet-Diffuser Ejector," *Journal of Aircraft*, Vol. 18, No. 12, 1981, pp. 1011–1018.

[3] Alperin, M., and Wu, J., "Thrust Augmenting Ejectors, Part I," *AIAA Journal*, Vol. 21, No. 10, 1983, pp. 1428–1436.

[4] Dutton, J., and Carroll, B., "Optimal Supersonic Ejector Designs," *Journal of Fluids Engineering*, Vol. 108, Dec. 1986, pp. 414–420.

[5] Dutton, J., and Carroll, B., "Limitation of Ejector Performance Due to Exit Choking," *Journal of Fluids Engineering*, Vol. 110, March 1988, pp. 91–93.

[6] Billig, F. S., "Low-Speed Operation of an Integrated Rocket–Ram–Scramjet for a Transatmospheric Accelerator," *Developments in High-Speed-Vehicle Propulsion Systems*, Vol. 165, Progress in Astronautics and Aeronautics, AIAA, Reston, VA, 1996, pp. 51–103.

[7] Daines, R., and Segal, C., "Combined Rocket and Airbreathing Propulsion Systems for Space Launch Applications," *Journal of Propulsion and Power*, Vol. 14, No. 5, 1998, pp. 605–612.

[8] Han, S., Peddieson, J., and Gregory, D., "Ejector Primary Flow Molecular Weight Effects in an Ejector–Ram Rocket Engine," *Journal of Propulsion and Power*, Vol. 18, No. 3, 2002, pp. 592–599.

[9] Cramer, J. M., Greene, M., Pal, S., and Santoro, R. J., "RBCC Ejector Mode Operating Characteristics for Single and Twin Thruster Configurations," AIAA Paper 2001-3464, 2001.

[10] West, J., Ruf, J., Cramer, J., Pal, S., and Santoro, R., "Computational Insight to Experimentally Observed Change in Mixing Characteristics of an RBCC Engine in Ejector Mode," AIAA Paper 2001-3459, 2001.

[11] Ruf, J. H., "Benchmark of FDNS CFD Code for Direct Connect RBCC Test Data," AIAA Paper 2000-36875, 2000.

[12] Daines, R. L., and Merkle, C. L., "Computational Analysis of Mixing and Jet Pumping in Rocket Ejector Engines," AIAA Paper 95-2477, 1995.

[13] DeBonis, J., and Yungster, S., "Rocket-Based Combined Cycle Engine Technology Development: Inlet CFD Validation and Application," AIAA Paper 96-3145, 1996.

[14] Daines, R. L., "Numerical Analysis of High-Frequency Jet-Switching on Dynamic Ejector Flowfields," AIAA Paper 97-2757, 1997.

[15] Daines, R. L., and Bulman, M., "Computational Analyses of Dynamic Rocket Ejector Flowfields," AIAA Paper 96-2686, 1996.

[16] Matesanz, A., Velazquez, A., Tizon, J., and Montanes, J., "Numerical Reconstruction of Ejector Rocket Experimental Tests," *Journal of Propulsion and Power*, Vol. 18, No. 6, 2002, pp. 1191–1198.

[17] Ristori, A., and Dufour, E., "Numerical Simulation of Ducted Rocket Motor," AIAA Paper 2001-3193, 2001.

[18] Steffen, C. J., Jr., Smith, T., Yungster, S., and Keller, D. J., "Computational Analysis for Rocket-Based Combined Cycle Systems During Rocket-Only Operation," *Journal of Propulsion and Power*, Vol. 16, No. 6, 2000, pp. 1030–1039.

[19] Stowe, R., Dubois, C., Harris, P., Mayer, A., Champlain, A. D., and Ringuette, S., "Two Phase Flow Combustion Modelling of a Ducted Rocket," AIAA Paper 2001-3461, 2001.

[20] Vanka, S., Craig, R., and Stull, F., "Mixing, Chemical Reaction, and Flowfield Development in Ducted Rockets," *Journal of Propulsion*, Vol. 2, July 1986, pp. 331–338.

[21] Parent, B., and Sislian, J. P., "The Use of Domain Decomposition in Accelerating the Convergence of Quasi-Hyperbolic Systems," *Journal of Computational Physics*, Vol. 179, No. 1, 2002, pp. 140–169.

[22] Parent, B., "Computational Study of Fuel Injection in a Scramjet Inlet," Ph.D. Dissertation, Inst. of Aerospace Studies, Univ. of Toronto, Toronto, 2002.

[23] Parent, B., and Sislian, J. P., "Validation of the Wilcox k–ω Model for Flows Characteristic to Hypersonic Airbreathing Propulsion," *AIAA Journal*, Vol. 42, No. 2, 2004, pp. 261–270.

[24] Etele, J., "Computational Study of Variable Area Ejector Rocket Flowfields," Ph.D. Dissertation, Inst. for Aerospace Studies, Univ. of Toronto, Toronto, 2004.

[25] Wilcox, D. C., "Dilatational–Dissipation Corrections for Advanced Turbulence Models," *AIAA Journal*, Vol. 30, No. 11, 1992, pp. 2639–2645.

[26] Goebel, S. G., and Dutton, J. C., "Experimental Study of Compressible Turbulent Mixing Layers," *AIAA Journal*, Vol. 29, No. 4, 1991, pp. 538–546.

[27] Cottrell, D. C., III, and Plesniak, M. W., "Sensitivity of Mixed Subsonic–Supersonic Turbulent Mixing Layers," *Journal of Propulsion and Power*, Vol. 17, No. 4, 2001, pp. 823–835.

[28] Wilcox, D. C., *Turbulence Modeling for CFD*, 2nd ed., DCW Industries, Inc., La Canada, California, 1998.

[29] Roache, P. J., "Verification of Codes and Calculations," *AIAA Journal*, Vol. 36, No. 4, 1998, pp. 696–702.

[30] Barber, T., Chiappetta, L., DeBonis, J., Georgiadis, N., and Yoder, D., "Assessment of Parameters Influencing the Prediction of Shear-Layer Mixing," *Journal of Propulsion and Power*, Vol. 15, No. 1, 1998, pp. 45–53.